RSC Advances

PAPER

View Article Online
View Journal | View Issue

Cite this: *RSC Adv.*, 2017, 7, 53847

Construction of C_{60}-decorated SWCNTs (C_{60}-CNTs)/bismuth-based oxide ternary heterostructures with enhanced photocatalytic activity†

Xue Lin, Yang Xi, Rui Zhao, Junyou Shi * and Ning Yan*

Received 8th October 2017
Accepted 13th November 2017

DOI: 10.1039/c7ra11056a

rsc.li/rsc-advances

Novel nanostructured carbon/$BiVO_4$ and nanostructured carbon/Bi_2MoO_6 nanocomposite photocatalysts were fabricated *via* a facile hydrothermal process by using fullerene (C_{60})-decorated single-walled carbon nanotubes (SWCNTs) as the carbon source, which are denoted as C_{60}-CNTs. The fabricated nanocomposites were characterized by various analytical techniques. The results showed that the C_{60}-CNTs are intimately bound to the bismuth-based oxide surfaces. The UV-vis diffuse reflectance spectra of C_{60}-CNTs/bismuth-based oxide nanocomposites exhibited increased visible-light absorption compared to pure bismuth-based oxides. Moreover, the ternary nanocomposites demonstrated significantly enhanced photocatalytic activity for the degradation of rhodamine B (Rh B) under visible light. The enhanced performance is attributed to the extended absorption in the visible-light region resulting from the incorporation of C_{60}-CNTs, high specific surface area, and efficient separation of electron–hole pairs by the ternary composite system. In addition, the radical-trapping experiments revealed that the holes and $O_2^{\bullet-}$ play major roles in the decolorization of Rh B under visible-light irradiation.

1. Introduction

Semiconductor photocatalysis is a promising environmental remediation technology that can be used to treat inorganic or organic pollutants in the environment.[1–3] To date, many semiconductor photocatalysts have been studied for use in water splitting and/or environmental remediation.[4–6] Among them, bismuth-based semiconductors (*e.g.*, Bi_2WO_6, $BiVO_4$, $Bi_4Ti_3O_{12}$, $Bi_2O_2CO_3$, BiOI and Bi_2MoO_6) have attracted great attention due to their many advantages, such as superior photocatalytic performance under UV and visible light irradiation, unique layered structures, resistance to photocorrosion, chemical stability, low/non-toxicity, and abundance in the earth.[7–12] Among the various bismuth-based semiconductors, $BiVO_4$ with a band gap of around 2.40 eV is a strong candidate because of its properties that include good photoconductivity and significant visible-light response.[13,14] However, some researches have revealed that the photocatalytic activity of pure $BiVO_4$ is comparatively low due to the difficulty in the separation of photogenerated electron–hole pairs.[14] Bi_2MoO_6, with excellent intrinsic physical and chemical properties, exhibits photocatalytic activity for water splitting and organic pollutant degradation.[15,16] Nevertheless, pure Bi_2MoO_6 itself has been a bit of a disappointment as a photocatalyst due to the fast recombination of the photo-induced electrons and holes in the material. Much work is centered on methods that can transform $BiVO_4$ or Bi_2MoO_6 into a more efficient visible light photocatalytic material.[17–19] Among the various methods, the construction of composite photocatalysts has shown to be an effective approach for improving the photocatalytic efficiency for the degradation of organic contaminants.[19]

In recent years, carbonaceous materials such as activated carbon (AC), carbon dots (CDots), fullerene (C_{60}), carbon nanotubes (CNTs) and graphene have been widely employed for the enhancement of photocatalytic performances of semiconductors, which has thus attracted considerable attention.[19,20] Carbon nanostructured materials have been used as coupling materials for bismuth-based composites due to their excellent electron accepting and electron-transporting properties.[20] Over the past few years, combination of two kinds of carbon materials such as C_{60}-CNTs, C_{60}-RGO, and GO-CDots as a new class of carbon nanostructured materials has attracted much attention due to their extraordinary electronic, optical, and chemical properties.[21,22] Moreover, there are many reports on composites containing SWCNTs and C_{60} clusters, which are known to decorate the SWCNT sidewall through covalent or noncovalent interaction.[21] Although MWCNTs, SWCNTs, and C_{60} have been widely investigated for coupling with semiconductor materials, studies on the photoactivity of the above-

---

College of Forestry, Beihua University, Jilin 132013, China. E-mail: bhsjy64@163.com; Fax: +86 432 6460 8076; Tel: +86 156 9434 9717

† Electronic supplementary information (ESI) available. See DOI: 10.1039/c7ra11056a

mentioned novel C_{60}-CNTs hybrid carbon materials coupled with bismuth-based oxides are still scarce, and the photocatalytic mechanism of the composite photocatalyst remains unclear.

Herein, we report two novel C_{60}-CNTs/bismuth-based oxide composite photocatalysts fabricated through sensitizing leaf-like $BiVO_4$ and sheet-like Bi_2MoO_6 with C_{60}-CNTs hybrid carbon materials *via* a facile hydrothermal method for the first time. The photocatalytic performances of the composites were examined by degrading rhodamine B (Rh B) under visible-light irradiation ($\lambda > 420$ nm). The experimental results showed that the as-prepared C_{60}-CNTs/bismuth-based oxide composites exhibited excellent photocatalytic activity. Moreover, the possible photocatalytic mechanism of the composite materials related to the band positions of the semiconductors have also been discussed in detail.

2. Experimental section

2.1 Preparation of photocatalysts

2.1.1 Preparation of C_{60}-CNTs. All reagents for synthesis and analysis were commercially available and used without further treatments. C_{60}-CNTs hybrids were prepared by using the Zhang's method:[21] 50 mg of SWCNTs and 50 mg of C_{60} were dispersed by ultrasonication in 100 mL toluene for 1 h, and then stirred at room temperature for 12 h. After volatilization of toluene, the resultant black powder was washed with ethanol for several times and dried in vacuum at 80 °C for 12 h to obtain the C_{60}-decorated SWCNTs (50 wt% C_{60}-CNTs, denoted as C_{60}-CNTs).

2.1.2 Preparation of C_{60}-CNTs/$BiVO_4$ and C_{60}-CNTs/Bi_2MoO_6. The nanostructured carbon/bismuth-based oxide nanocomposites were prepared by a hydrothermal method. For example, in a typical synthetic process for nanostructured carbon/$BiVO_4$, 15 mg of C_{60}-CNTs was dispersed in 15 mL water by sonication, and $Bi(NO_3)_3 \cdot 5H_2O$ (0.88 mmol) and NH_4VO_3 (0.88 mmol) were added to the mixture and stirred for additional 1 h at room temperature. The theoretical weight ratio of C_{60}-CNTs to $BiVO_4$ was 1 : 19 for the nanostructured carbon/$BiVO_4$ (2.5 wt% C_{60}/2.5 wt% CNTs/$BiVO_4$, denoted as C_{60}-CNTs/$BiVO_4$). After carefully adjusting the pH value to 3 using 25 wt% $NH_3 \cdot H_2O$ solution, the resulting mixture was transferred into a 20 mL Teflon-lined stainless steel autoclave and kept at 150 °C for 24 h. The obtained product was collected by centrifugation, washed with water and ethanol several times, and then dried at 80 °C overnight. C_{60}-CNTs/Bi_2MoO_6 was prepared *via* a similar process.

2.2 Characterization of photocatalysts

X-ray diffraction (XRD) was carried out on a D/MAX 2500V diffractometer (Rigaku, Japan) with monochromatized Cu K_α radiation, $\lambda = 0.154\ 18$ nm, in the 2θ range of 10 to 70°. The morphologies and microstructures of the products were characterized by transmission electron microscopy (TEM, JEM-2100F). X-ray photoelectron spectroscopy (XPS, VGScientific) using 300 W Al K_α radiation as the excitation source was applied to study the composition and chemical states of the elements. The FT-IR spectra were recorded on an FTIR spectrometer (America Perkin Elmer, Spectrum One) using the standard KBr disk method. UV-vis absorption spectra of the samples were tested on a scan UV-vis spectrophotometer (Shimadzu, UV-2550) equipped with an integrating sphere using $BaSO_4$ as the reference sample. The surface areas were measured by the nitrogen adsorption Brunauer–Emmett–Teller (BET) method (BET/BJH surface area, 3H-2000PS1). The photoluminescence (PL) spectra of the photocatalysts were obtained using a F4500 (Hitachi, Japan) photoluminescence detector with an excitation wavelength of 325 nm.

2.3 Photocatalytic activities studies

The photocatalytic properties of the as-prepared samples were evaluated using Rh B as a model compound. In the experiments, the Rh B solution (0.01 mmol L^{-1}, 100 mL) containing 0.02 g of photocatalyst was mixed in a pyrex reaction glass. The reactivity experiments were carried out in air at room temperature. A 300 W Xe lamp ($\lambda > 420$ nm) with 100 mW cm^{-2} illumination intensity was employed to provide visible-light irradiation. A 420 nm cut-off filter was inserted between the lamp and the sample to filter out UV light ($\lambda < 420$ nm). Prior to visible-light illumination, the suspension was strongly stirred in dark for 40 min. The solution was then exposed to visible-light irradiation under magnetic stirring. At specific time intervals, 4 mL of the suspension was periodically collected and analyzed after centrifugation. The Rh B concentration was analyzed using a UV-2550 spectrometer to record the intensity of the maximum band at 552 nm in the UV-vis absorption spectra.

2.4 Active species trapping experiments

To detect the active species during photocatalytic reactivity, some sacrificial agents such as 2-propanol (IPA), disodium ethylenediamine tetraacetic acid (EDTA-2Na), and 1,4-benzoquinone (BQ) were used as scavengers for hydroxyl radical ($^{\bullet}OH$), hole (h^+), and superoxide radical ($O_2^{\bullet-}$), respectively. The method was similar to the former photocatalytic activity test with the addition of 1 mmol of quencher in the presence of Rh B.

3. Results and discussion

The XRD patterns of SWCNTs, C_{60}, and C_{60}-CNTs are shown in Fig. 1a. In the diffraction pattern of SWCNTs, an apparent wide peak at $2\theta = \sim 26°$ appeared, corresponding to the (002) plane.[21] C_{60} exhibits diffraction peaks corresponding to (111), (220), (311), and (222) planes at $2\theta = 10.7°$, 17.7°, 20.7°, and 21.7°, which can be readily indexed to a face centered cubic (fcc) structure (JCPDS no. 44-558).[21] When the two compounds were coupled, the main characteristic diffraction peaks of SWCNTs and C_{60} exhibited no obvious change, indicating that C_{60} clusters in C_{60}-CNTs can form an fcc crystallite. Fig. 1b displays the XRD patterns of the bare Bi_2MoO_6 and C_{60}-CNTs/Bi_2MoO_6 composite. All the diffraction peaks in the pattern of Bi_2MoO_6 can be indexed to the specific crystal planes of the Bi_2MoO_6

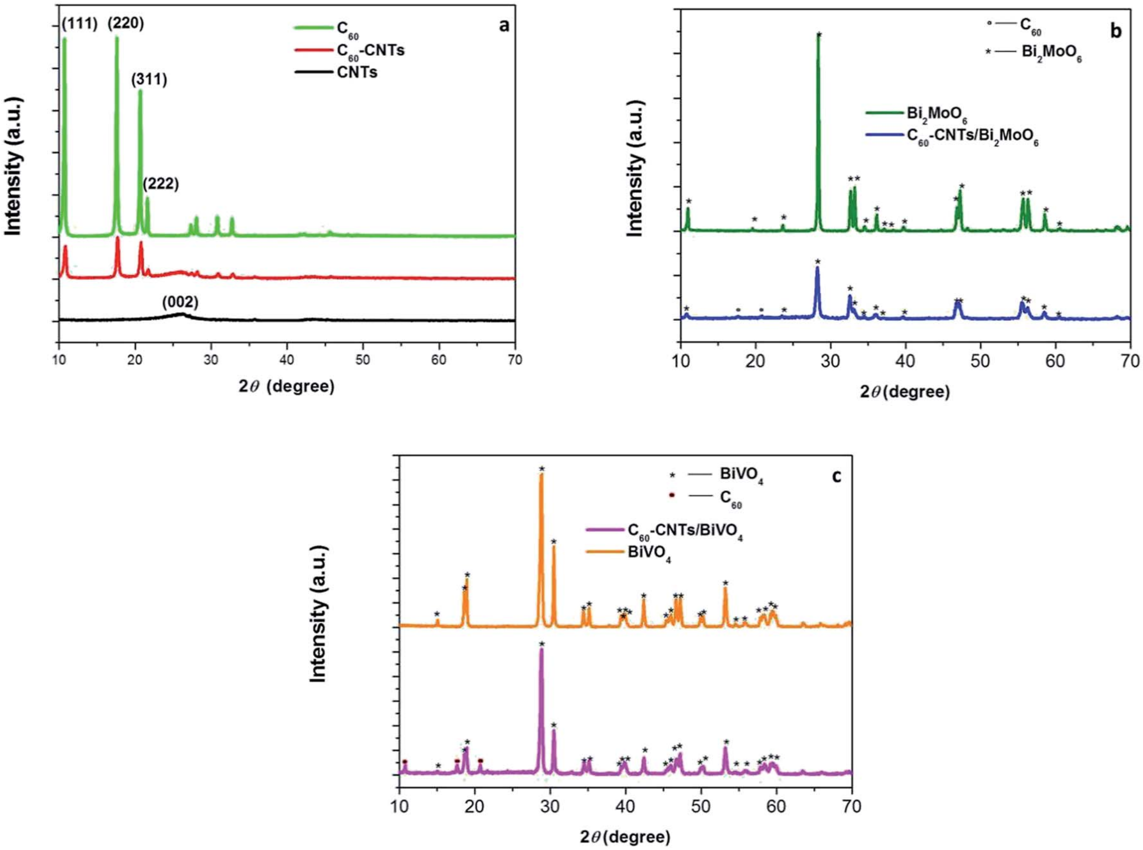

Fig. 1 XRD patterns of SWCNTs, C_{60} and C_{60}-CNTs (a), Bi_2MoO_6 and C_{60}-CNTs/Bi_2MoO_6 (b), and $BiVO_4$ and C_{60}-CNTs/$BiVO_4$ (c).

phase (JCPDS no. 21-0102). Besides the peaks of Bi_2MoO_6, the diffraction peaks of C_{60} in the pattern of C_{60}-CNTs/Bi_2MoO_6 can be observed, indicating the coexistence of C_{60}. Doping with SWCNTs did not significantly change the structure of Bi_2MoO_6. It was reported that SWCNTs show a weak but characteristic diffraction peak at 26.0°. However, this peak was not apparent in the patterns of the as-prepared composites, which could be attributed to the small amount of SWCNTs in the composites. In the C_{60}-CNTs/$BiVO_4$ composite, the diffraction peaks of $BiVO_4$ (JCPDS no. 14-0688) and C_{60} were detected (Fig. 1c), suggesting the existence of C_{60} and $BiVO_4$ phases.

Fig. 2 displays the microstructures of C_{60}-CNTs/$BiVO_4$ and C_{60}-CNTs/Bi_2MoO_6. Usually, the produced SWCNTs have a tendency to form tight bundles.[23,24] C_{60}-CNTs are also made of bundles of entangled SWCNTs. As shown in Fig. 2a, the C_{60}-CNTs are intimately bound to the leaf-like $BiVO_4$ nanostructure surfaces. However, some single or double SWCNTs with an average diameter of ~10 nm can still be observed (Fig. 2b). C_{60} molecules with a diameter of *ca.* 0.7 nm is too small to be directly resolved by HRTEM observation, which is similar to the reported work.[21] The lattice fringe pattern of $BiVO_4$ was measured as 0.224 nm (Fig. 2c), consistent with the interplanar spacing of the $BiVO_4$ (121) plane. A similar phenomenon occurred in the C_{60}-CNTs/Bi_2MoO_6 nanocomposite. As can be seen in Fig. 2d and e the C_{60}-CNTs are intimately bound to the surfaces of the Bi_2MoO_6 nanosheets. The lattice fringe pattern of Bi_2MoO_6 was measured as 0.38 nm (Fig. 2f), which is consistent with the interplanar spacing of the Bi_2MoO_6 (111) plane.

FTIR spectroscopy was applied to distinguish the microstructures of nanostructured carbons and their composites. Fig. 3a shows the FTIR spectra of C_{60}, CNTs, C_{60}-CNTs, C_{60}-CNTs/Bi_2MoO_6, and C_{60}-CNTs/$BiVO_4$. The bands at 1182, 1429, and 1630 cm^{-1} are attributed to the internal modes of the C_{60} molecule.[25] It can be observed that both C_{60}-CNTs/$BiVO_4$ and C_{60}-CNTs/Bi_2MoO_6 nanocomposites reveal the characteristic bands for C_{60} molecule, showing the existence of C_{60}-CNTs. The successful loading of C_{60}-CNTs was also illustrated by XPS. Fig. 3b displays the deconvolution of the C 1s peaks of C_{60}-CNTs, C_{60}-CNTs/Bi_2MoO_6, and C_{60}-CNTs/$BiVO_4$. For C_{60}-CNTs, the main peak at 282.3 eV was assigned to the sp^2-hybridized carbon of CNTs, which can be ascribed to the C–C bond of the sp^2-hybridized carbon in the graphene sheet. In case of C_{60}-CNTs/Bi_2MoO_6 and C_{60}-CNTs/$BiVO_4$, the binding energy of C 1s shifted by about 0.2 and 0.5 eV, respectively, toward higher binding energies. A similar phenomenon was observed for Bi 4f (Fig. 3c). This implied the successful incorporation of C_{60}-CNTs into Bi_2MoO_6 or $BiVO_4$. The spin-orbit of Bi 4f in Bi_2MoO_6 and $BiVO_4$ could be well deconvoluted as two peaks at around 159 and 164 eV, which correspond to the Bi $4f_{7/2}$ and Bi $4f_{5/2}$ orbits of Bi^{3+}, respectively.

Fig. 4a shows the UV-vis absorption spectra of bare Bi_2MoO_6, $BiVO_4$, C_{60}-CNTs, and C_{60}-CNTs/Bi_2MoO_6, and C_{60}-CNTs/$BiVO_4$

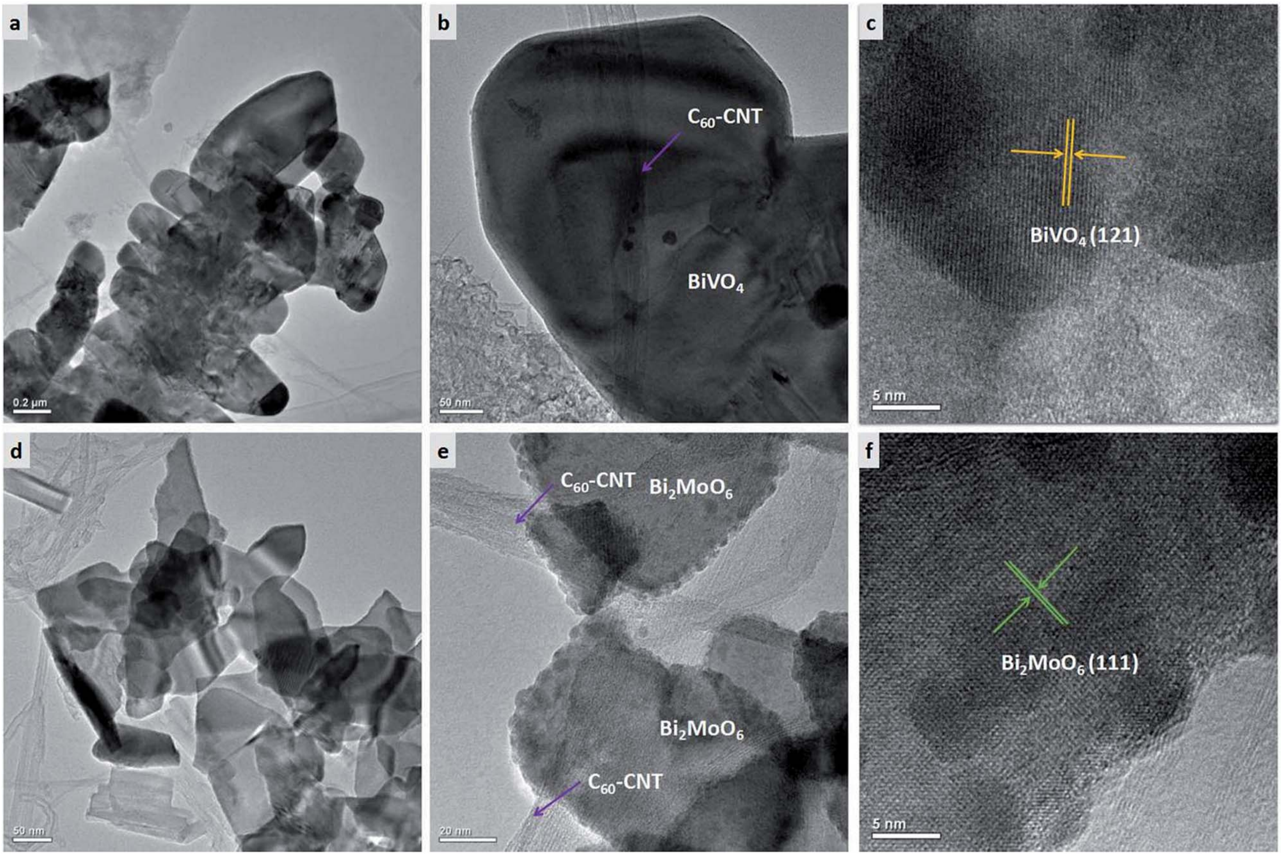

Fig. 2 TEM images of as-prepared samples: (a, b) C_{60}-CNTs/$BiVO_4$, (c) HRTEM image of C_{60}-CNTs/$BiVO_4$, (d, e) C_{60}-CNTs/Bi_2MoO_6, (f) HRTEM image of C_{60}-CNTs/Bi_2MoO_6.

nanocomposites. All the samples exhibit the typical absorptions with an intense transition in the visible region. In addition, the introduction of nanostructured carbons (C_{60}-CNTs) into the Bi_2MoO_6 or $BiVO_4$ leads to an increase in absorption in the visible-light region, indicating an intense electronic interaction between the bismuth-based oxide and nanostructured carbon, when C_{60}-CNTs were used as the carbon source.[21]

In general, for a crystalline semiconductor, the optical absorption band edge can be estimated according to the formula, $\alpha h\nu = A(h\nu - E_g)^{n/2}$, where α, ν, E_g, and A are the absorption coefficient, light frequency, band-gap energy, and a constant, respectively. Among these parameters, n is determined by the type of optical transition in a semiconductor. The value of n is 1 for direct transition and 4 for indirect transition. For Bi_2MoO_6 or $BiVO_4$, the value of n is 1 for direct transition, thus, the band gaps were estimated as about 2.34 eV for $BiVO_4$ and 2.53 eV for Bi_2MoO_6, as shown in Fig. 4b. In addition, the potentials of the valence band (VB) and conduction band (CB) for $BiVO_4$ can be calculated according to the two formulas which are proposed by Butler and Ginley:

$$E_{VB} = X - E^e + 0.5E_g \quad (1)$$

$$E_{CB} = E_{VB} - E_g \quad (2)$$

Here, E_{VB} is the valence band edge potential, E_{CB} is the conduction band edge potential, X is the electronegativity of the semiconductor, which is the geometric mean of the electronegativity of the constituent atoms, E^e is the energy of free electrons on the hydrogen scale (about 4.5 eV), and E_g is the band gap energy of the semiconductor. Based on the above formulas, the VB potential and CB potential of $BiVO_4$ were calculated as 2.828 eV and 0.488 eV, respectively, whereas the CB and VB edge potentials of Bi_2MoO_6 were −0.26 eV and 2.27 eV, respectively.

The photocatalytic activities of the samples were evaluated by photocatalytic degradation of a Rh B solution under visible light. Adsorption equilibrium was reached for all the examined photocatalysts after stirring for 40 min in dark (Fig. S1†). As can be seen in Fig. 5a, when the solution is irradiated with visible light for 30 min in the absence of any catalyst, little change in Rh B concentration is observed, which is in agreement with previous reports.[26,27] This indicates that the self-photodegradation of Rh B is negligible. As shown in Fig. 5a, pure Bi_2MoO_6 and $BiVO_4$ exhibited generally low photocatalytic activities, with only 43.7% and 74.0% Rh B degradation, respectively, after visible-light irradiation for 30 min. This low performance is possibly due to the fast recombination of photo-induced electrons and holes in the single semiconductor. The results indicate that the photocatalytic activity of C_{60}-CNTs/

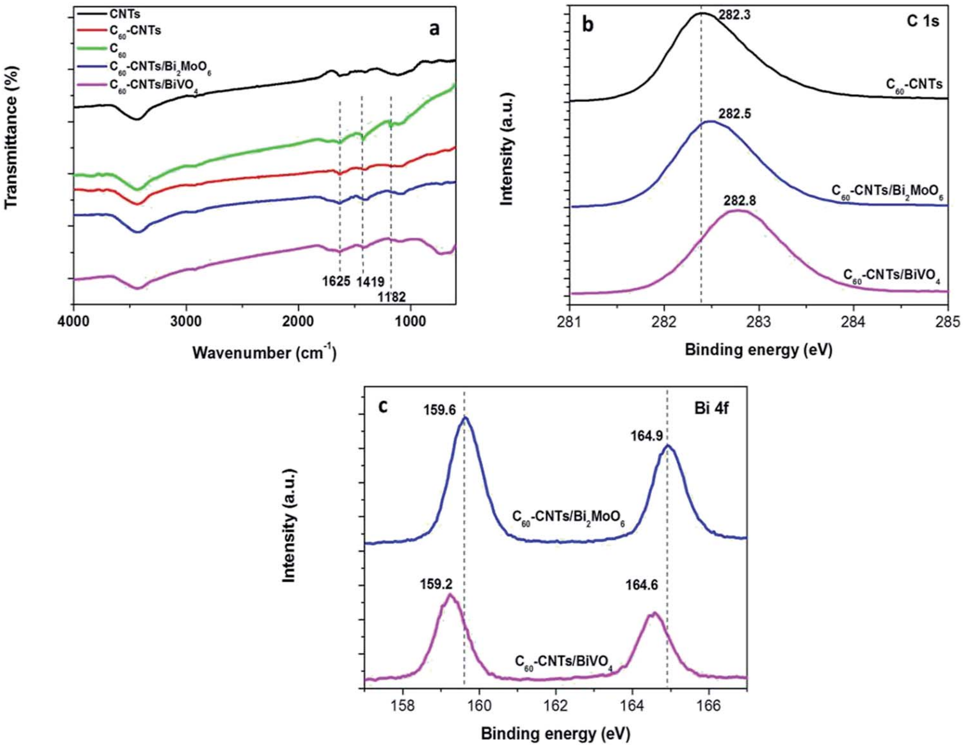

Fig. 3 (a) FTIR of as-prepared samples. XPS spectra of as-obtained samples: (b) C 1s, (c) Bi 4f.

bismuth-based oxide nanocomposites toward Rh B is much higher than that of either pure Bi_2MoO_6 or $BiVO_4$. The introduction of C_{60}-CNTs to bismuth-based oxides resulted in significant improvement in the photocatalytic performances of Bi_2MoO_6 and $BiVO_4$. After 30 min of visible-light irradiation, the photocatalytic degradation percentages of Rh B were about 96.1% and 88.4% for C_{60}-CNTs/$BiVO_4$ and C_{60}-CNTs/Bi_2MoO_6 composites, respectively. This is because the efficient heterojunction interface between two or three components can restrain the recombination of photo-induced charges effectively.[28,29] The C_{60}-CNTs coating can improve the visible-light absorption efficiency (Fig. 4), which is beneficial for the ternary composite in photolyzing Rh B.[30,31] Further, the surface areas of the samples were measured by N_2 adsorption–desorption isotherms. Fig. 5b shows the N_2 adsorption–desorption isotherms at 77 K. The obtained BET specific surface areas for $BiVO_4$, Bi_2MoO_6, C_{60}-CNTs, C_{60}-CNTs/$BiVO_4$, and C_{60}-CNTs/Bi_2MoO_6 samples are 20.913, 44.202, 188.426, 146.071, and 179.465 $m^2\ g^{-1}$, respectively (Table 1). It can be observed that the BET specific areas increased after the loading of C_{60}-CNTs, which can facilitate more efficient contact of the composite samples with organic contaminants, leading to the enhancement of photocatalytic efficiency.[32,33] Because a renewable catalyst is another important criterion for photocatalytic application,[34] the stabilities of C_{60}-CNT/Bi_2MoO_6 and C_{60}-CNTs/$BiVO_4$ composites were investigated by a recycling test (Fig. 5c).

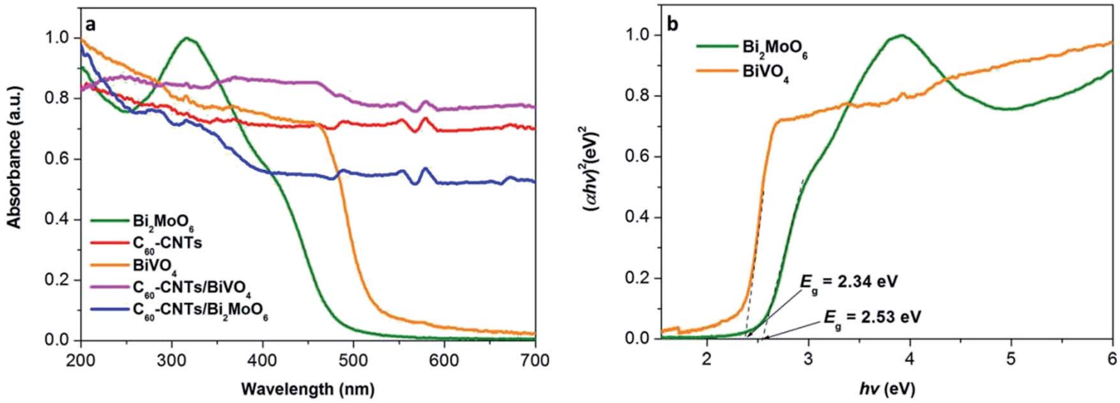

Fig. 4 (a) UV-vis absorption spectra of the as-obtained samples. (b) Plots of $(\alpha h\nu)^2$ *versus* photon energy ($h\nu$) for the band gap energies of $BiVO_4$ and Bi_2MoO_6.

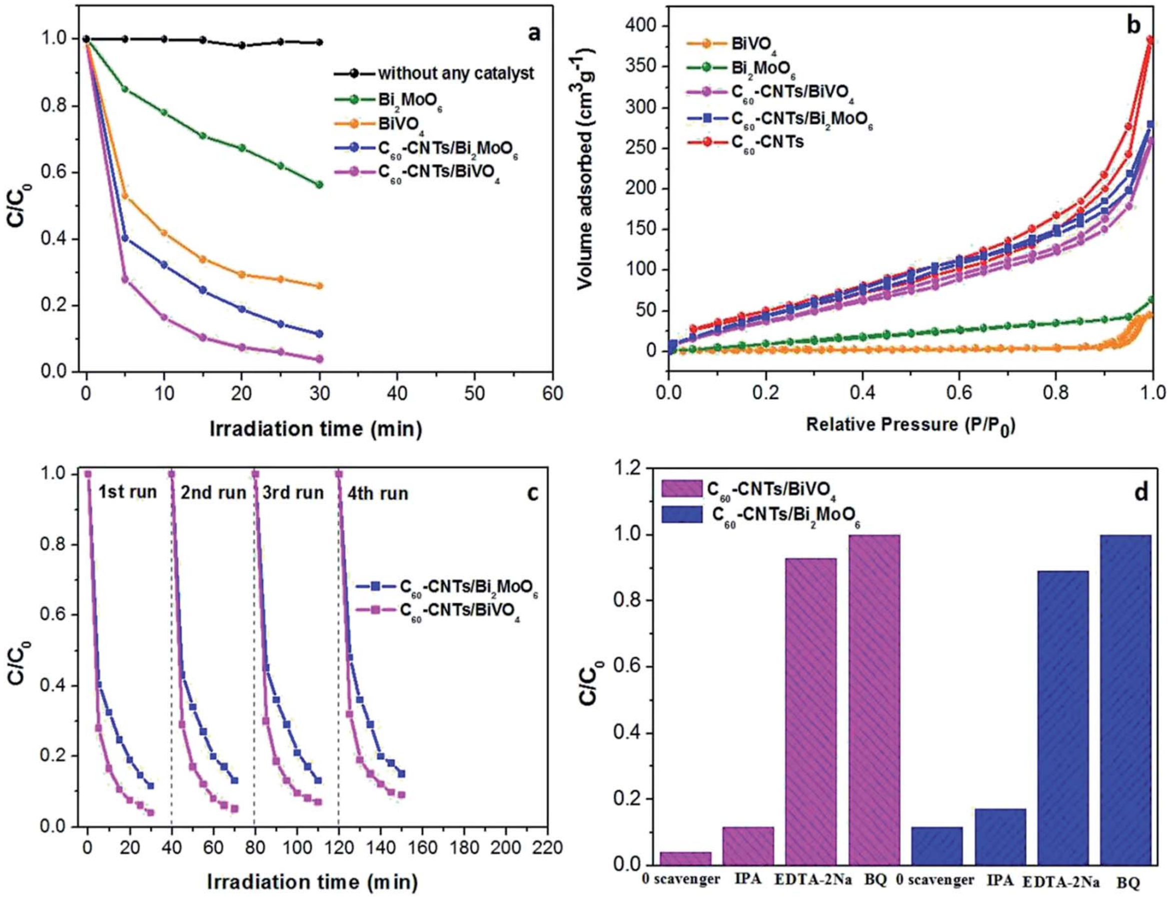

Fig. 5 (a) Photodegradation efficiencies of Rh B as a function of irradiation time for different photocatalysts. (b) N_2 adsorption–desorption isotherm curves of the as-prepared samples. (c) Cycling runs for photocatalytic degradation of Rh B over the ternary nanocomposites under visible-light irradiation. (d) Trapping experiment of active species during photocatalytic degradation of Rh B over C_{60}CNTs/bismuth-based oxide nanocomposites under visible-light irradiation.

After four cycles, there was no significant loss of activity, which indicated that the composite photocatalysts were stable during the photocatalytic test.

To further probe the underlying mechanism of the ternary nanocomposites, different scavengers for the various active species were added into the reaction system. In particular, IPA, BQ, and EDTA-2Na were used to capture $^{\bullet}OH$, $^{\bullet}O^{2-}$, and h^+, respectively. As shown in Fig. 5d, the photocatalytic performance of C_{60}-CNTs/Bi_2MoO_6 toward Rh B degradation was clearly inhibited by the addition of EDTA-2Na and BQ. Similar results were observed with the trapping of active species during the photocatalytic degradation of Rh B over C_{60}-CNTs/$BiVO_4$. These results indicate that $^{\bullet}O^{2-}$ and h^+ play critical roles in the photocatalytic degradation of Rh B for the ternary composites.

The possible photocatalytic mechanism of the C_{60}-CNTs/Bi_2MoO_6 nanocomposite is illustrated in Fig. 6. First, the large specific surface areas of the ternary nanocomposite and its enhanced adsorption ability toward the contaminants contribute to the photocatalytic process. Particularly, the loading of C_{60}-CNTs promotes the visible-light absorption of Bi_2MoO_6, which enables photoexcitation of more electrons from the VB to the CB.[21] Further, the small C_{60} molecules can serve as an efficient electron reservoir to capture the photogenerated electrons, thus hindering the recombination of electron–hole carriers.[22] Meanwhile, CNTs can also help to suppress the charge recombination by capturing the photogenerated electrons owing to their excellent electron conductivity and mobility.[23] On the other hand, owing to the formation of

Table 1 BET specific surface area of the as-prepared samples

Photocatalysts	BET specific surface area (m^2 g^{-1})	Photocatalysts	BET specific surface area (m^2 g^{-1})
$BiVO_4$	20.913	C_{60}-CNTs/$BiVO_4$	146.071
Bi_2MoO_6	44.202	C_{60}-CNTs/Bi_2MoO_6	179.465
C_{60}/CNTs	188.426		

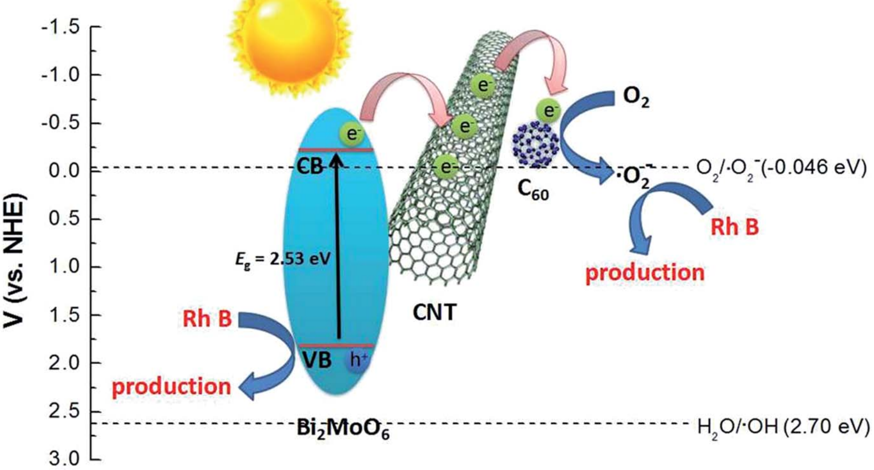

Fig. 6 Schematic diagram of the separation and transfer of photogenerated charges in the C_{60}-CNTs/Bi_2MoO_6 composite photocatalyst under visible-light irradiation.

heterojunctions between C_{60}-CNTs and Bi_2MoO_6 and their intimate interfacial interaction, photogenerated electrons can efficiently transfer to C_{60} and CNTs, thus showing enhanced separation efficiency for the photogenerated holes–electrons pairs. In this way, the excited electrons participate in the reduction of O_2 to $^{\bullet}O^{2-}$. Subsequently, the $^{\bullet}O^{2-}$ and holes on the valence band of Bi_2MoO_6 oxidize the Rh B to CO_2 and H_2O.

4. Conclusions

In this study, C_{60}-decorated SWCNTs (C_{60}-CNTs) were prepared by a solution method. Thereafter, novel nanostructured carbon/bismuth-based oxide nanocomposites were successfully synthesized *via* a facile hydrothermal method with nanostructured carbons. These nanostructured carbon/bismuth-based oxide nanocomposites are beneficial for improving the photocatalytic efficiency. The enhanced performance is due to the extended absorption in the visible-light region resulting from C_{60}-CNTs loading, high specific surface area, and efficient separation of electron–hole pairs by the ternary composite system. This study suggests that the C_{60}-CNTs, as a new carbon nanostructured material, can be employed as an effective co-catalyst for photocatalytic application.

Conflicts of interest

There are no conflicts to declare.

Acknowledgements

This work was supported by the Project of State Forestry Administration of China (201504502), the National Natural Science Foundation of China (21407059) and the Open Subject of the State Key Laboratory of Rare Earth Resource Utilization (RERU2017011).

References

1 B. Qiu, M. Xing and J. Zhang, *J. Am. Chem. Soc.*, 2014, **136**, 5852–5855.
2 P. P. Gai, R. B. Song, C. Zhu, Y. S. Ji, Y. Chen, J. R. Zhang and J. J. Zhu, *Chem. Commun.*, 2015, **51**, 14735–14738.
3 W. B. Li, C. Feng, S. Y. Dai, J. G. Yue, F. X. Hua and H. Hou, *Appl. Catal., B*, 2015, **168**, 465–471.
4 J. N. Hui, G. Zhang, C. S. Ni and J. T. S. Irvine, *Chem. Commun.*, 2017, **53**, 10038–10041.
5 R. C. Pawar and C. S. Lee, *Appl. Catal., B*, 2014, **144**, 57–65.
6 K. A. Tsai and Y. J. Hsu, *Appl. Catal., B*, 2015, **164**, 271–278.
7 Z. F. Huang, L. Pan, J. J. Zou, X. W. Zhang and L. Wang, *Nanoscale*, 2014, **6**, 14044–14063.
8 D. F. Hou, X. L. Hu, P. Hu, W. Zhang, M. F. Zhang and Y. H. Huang, *Nanoscale*, 2013, **5**, 9764–9772.
9 T. T. Li, X. L. Hu, C. C. Liu, C. M. Tang, X. K. Wang and S. L. Luo, *J. Mol. Catal. A: Chem.*, 2016, **425**, 124–135.
10 N. Liang, M. Wang, L. Jin, S. S. Huang, W. L. Chen, M. Xu, Q. Q. He, J. T. Zai, N. H. Fang and X. F. Qian, *ACS Appl. Mater. Interfaces*, 2014, **6**, 11698–11705.
11 J. C. Wang, H. C. Yao, Z. Y. Fan, L. Zhang, J. S. Wang, S. Q. Zang and Z. J. Li, *ACS Appl. Mater. Interfaces*, 2016, **8**, 3765–3775.
12 S. Yuan, Y. Zhao, W. B. Chen, C. Wu, X. Y. Wang, L. N. Zhang and Q. Wang, *ACS Appl. Mater. Interfaces*, 2017, **9**, 21781–21790.
13 L. Zhou, Y. Yang, J. Zhang and P. M. Rao, *ACS Appl. Mater. Interfaces*, 2017, **9**, 11356–11362.
14 T. Saison, N. Chemin, C. Chanéac, O. Durupthy, L. Mariey, F. Maugé, V. Brezová and J. P. Jolivet, *J. Phys. Chem. C*, 2015, **119**, 12967–12977.
15 Y. C. Hao, X. L. Dong, S. R. Zhai, X. Y. Wang, H. C. Ma and X. F. Zhang, *RSC Adv.*, 2016, **6**, 35709–35718.
16 S. J. Li, X. F. Shen, J. S. Liu and L. S. Zhang, *Environ. Sci.: Nano*, 2017, **4**, 1155–1167.

17 S. N. Lou, J. Scott, A. Iwase, R. Amal and Y. H. Ng, *J. Mater. Chem. A*, 2016, **4**, 6964–6971.

18 T. Yan, Q. Yan, X. D. Wang, H. Y. Liu, M. M. Li, S. X. Lu, W. G. Xu and M. Sun, *Dalton Trans.*, 2015, **44**, 1601–1611.

19 J. S. Cai, J. Y. Huang and Y. K. Lai, *J. Mater. Chem. A*, 2017, **5**, 16412–16421.

20 J. L. Li, X. J. Liu, X. Q. Piao, Z. Sun and L. K. Pan, *RSC Adv.*, 2015, **5**, 16592–16597.

21 B. Chai, T. Y. Peng, X. H. Zhang, J. Mao, K. Li and X. G. Zhang, *Dalton Trans.*, 2013, **42**, 3402–3409.

22 B. Chai, X. Liao, F. Song and H. Zhou, *Dalton Trans.*, 2014, **43**, 982–989.

23 L. F. Yue, S. F. Wang, G. Q. Shan, W. Wu, L. W. Qiang and L. Y. Zhu, *Appl. Catal., B*, 2015, **176–177**, 11–19.

24 S. Reddy, R. Du, L. X. Kang, N. N. Mao and J. Zhang, *Appl. Catal., B*, 2016, **194**, 16–21.

25 J. G. Yu, T. T. Ma, G. Liu and B. Cheng, *Dalton Trans.*, 2011, **40**, 6635–6644.

26 H. P. Li, J. Y. Liu, W. G. Hou, N. Du, R. J. Zhang and X. T. Tao, *Appl. Catal., B*, 2014, **160–161**, 89.

27 H. Q. Pan, X. K. Li, Z. J. Zhuang and C. Zhang, *J. Mol. Catal. A: Chem.*, 2011, **345**, 90.

28 S. Juntrapirom, D. Tantraviwat, S. Suntalelat, O. Thongsook, S. Phanichphant and B. Inceesungvorn, *J. Colloid Interface Sci.*, 2017, **504**, 711–720.

29 S. J. Li, S. W. Hu, K. B. Xu, W. Jiang, Y. Liu and Z. Leng, *J. Colloid Interface Sci.*, 2017, **504**, 561–569.

30 Y. L. Qi, Y. F. Zheng, H. Y. Yin and X. C. Song, *J. Alloys Compd.*, 2017, **712**, 535–542.

31 Q. Z. Luo, X. L. Yang, X. X. Zhao, D. S. Wang, R. Yin, X. Y. Li and J. An, *Appl. Catal., B*, 2017, **204**, 304–315.

32 Y. R. Zhao, J. Z. Ma, J. L. Liu and Y. Bao, *Colloids Surf., A*, 2017, **518**, 57–63.

33 Y. Q. Yang, W. K. Zhang, R. X. Liu, J. M. Cui and C. Deng, *Sep. Purif. Technol.*, 2018, **190**, 278–287.

34 Y. F. Zhang, M. Park, H. Y. Kim and S. J. Park, *J. Alloys Compd.*, 2016, **686**, 106–114.